

---

# INTEGRATION OF SOLID-STATE NANOPORE ARRAYS VIA DRY BONDING TO PHOTOSTRUCTURED MICROFLUIDIC NETWORKS

---

A PREPRINT

 **Peter D. Jones**

NMI Natural and Medical Sciences Institute  
at the University of Tübingen  
72770 Reutlingen  
Germany  
peter.jones@nmi.de

 **Michael Mierzejewski**

NMI Natural and Medical Sciences Institute  
at the University of Tübingen  
72770 Reutlingen  
Germany  
michael.mierzejewski@nmi.de

September 23, 2024

## ABSTRACT

The integration and parallelization of nanopore sensors are essential for improving the throughput of nanopore measurements. Solid-state nanopores traditionally have been used in isolation, which prevents the realization of their full potential in applications. In this study, we present the microfluidic integration of an array of 30 nanopores, which, to our knowledge, is the highest number reported to date. Our microfluidic network was fabricated using high-resolution epoxy photoresists, and the solid-state membranes were bonded through a dry process using complementary surface chemistries. We successfully measured integrated nanopores using external electrodes. This paper discusses the limitations of our methods, particularly concerning microfluidic interfacing and scaling to higher channel counts. Additionally, we present theoretical analysis of current blockades and noise in integrated nanopores, predicting that maintaining low series resistance between the nanopore and electrode is crucial for resolving short events.

**Keywords** nanopore sensors · microfluidic · dry bonding · hybrid integration · impedance spectroscopy

## 1 Introduction

Nanopore sensors have an enormous potential. Commercial success has been achieved with biological nanopores, while promising basic research with solid-state nanopores remains to be translated into practical use. Parallelization has proven to be an important factor for efficient research on biological nanopores and is critical for practical use [Laszlo et al., 2014]. Examples include the hundreds of nanopores per Oxford Nanopore Technologies flow cell (5 kHz bandwidth) or the sixteen nanopores in Ionera microelectrode-cavity array (MECA) chips (100 kHz bandwidth with Nanion systems). In contrast, a key weakness of solid-state nanopores is their measurement as single pores. Few works integrate multiple solid-state nanopores (Table 1).

A primary challenge for arrays of solid-state nanopores is the filling of the trans compartment with salt solution, while maintaining isolation between neighboring nanopores [Magierowski et al., 2016]. Consider biological nanopores: the trans compartments are initially wetted during filling of a common cis compartment. Thereafter, formation of a lipid bilayer encloses the trans compartments and forms an insulating membrane. Biological nanopores then spontaneously enter the membrane. In contrast, solid-state membranes of silicon nitride or other engineering materials cannot be spontaneously formed in place. The trans compartments must therefore be filled by another means. Good methods for wetting the trans compartments of an array of solid-state nanopores should have the capacity to be scaled to at least hundreds of pores to compete with biological nanopores, and must be user-friendly to be viable for envisioned applications.

A pioneering work integrated solid-state nanopores in PDMS microfluidics by transfer printing of free-standing membranes [Jain et al., 2013]. Other works have similarly bonded membranes supported by a silicon frame to

Table 1: Overview of microfluidic integration of solid-state nanopores.

Number of nanopores	Details	Fluidic interfacing	Reference
1	Nanopore chip assembled with silicone	Reservoir on both sides	Rosenstein et al. [2012]
1	SiN membrane sandwiched between PDMS	One channel on each side of the membrane	Jain et al. [2013]
5	Nanopore chip sandwiched between PDMS	Five channels / shared channel	Tahvildari et al. [2015]
5	Nanopore chip sandwiched between PDMS	Five channels with microfluidic valves / shared channel	Tahvildari et al. [2016]
8	SiN membrane sandwiched between PDMS	Eight channels with microfluidic valves / shared channel	Jain et al. [2017]
30	Bonded on one side to epoxy channels	Thirty channels / open reservoir	This work

PDMS microfluidics [Tahvildari et al., 2015, 2016]. Disadvantages of PDMS include its poor compatibility with microfabrication processes, its capacity to absorb small molecules, and its hydrophobicity. PDMS microfluidics also do not easily allow electrodes near the integrated nanopores.

These works achieved poor usability, as each nanopore is in its own microfluidic channel. To simplify this, integration of microfluidic valves in PDMS has been demonstrated [Tahvildari et al., 2016, Jain et al., 2017]. Jain et al. discussed how the higher possible density of nanopores vs. density of electrodes and amplifiers supports the use of fluidic switching of nanopores. They used a three-bit multiplexer to address eight channels, demonstrating how microfluidic valves can allow higher density of nanopores and reduce the number of fluidic connections. For a given number of nanopores, the number of pneumatic channels is the binary logarithm. Further development to integrate individual electrodes for each nanopores, use alternative elastomeric materials instead of PDMS, and to increase the number of channels would make this a promising concept.

Nanopore array fabrication methods must also be developed. While the smallest nanopores are produced by electron beam milling in a transmission electron microscope (TEM), this method is poorly suited for arrays. Ion beam milling in a helium ion microscope (HIM) provides very small nanopore sizes and better scalability [Emmrich et al., 2016, Xia et al., 2018]. Controlled breakdown has been demonstrated with microfluidic integration [Tahvildari et al., 2015]. The most scalable method would likely be reactive-ion etching (RIE) [Bai et al., 2014, Martens et al., 2022]. Beyond parallelization, integration can reduce noise in nanopore sensors [Rosenstein et al., 2012, Jain et al., 2013].

Here, we present a new concept for microfluidic integration of nanopore arrays in permanent epoxy-based microfluidics (Figure 1). While originally developed towards the application of nanofluidic chemical neurostimulation [Jones, 2017], the concept and fabrication methods are promising for nanopore sensors. Our microfluidic structures with a thickness below 30  $\mu\text{m}$  are compatible with substrate-integrated microelectrodes on glass or silicon. We demonstrate the permanent bonding of solid-state membranes with 30 focused-ion-beam-milled nanopores. Bonding is performed after independent microfabrication (of electrodes and microfluidics) and nanofabrication (of nanopores) to maximize process flexibility. We present electrochemical measurements and calculations demonstrating potential noise reductions with our integrated arrays.

We furthermore discuss limitations of our nanopore array devices, including poor user-friendliness (with a custom 60-tube microfluidic connector). The need for two tubes per nanopore limits scalability. Our demonstration used large nanopores milled by a gallium beam and measured with external electrodes, rather than integrated microelectrodes.

Despite these limitations, our methods should enable fabrication of nanopore arrays if new concepts can solve the microfluidic interfacing and usability issues. Separation of micro- and nanofabrication enables compatibility with nanopore fabrication by methods such as milling with focused electron or ion beams, reactive-ion etching or controlled breakdown.

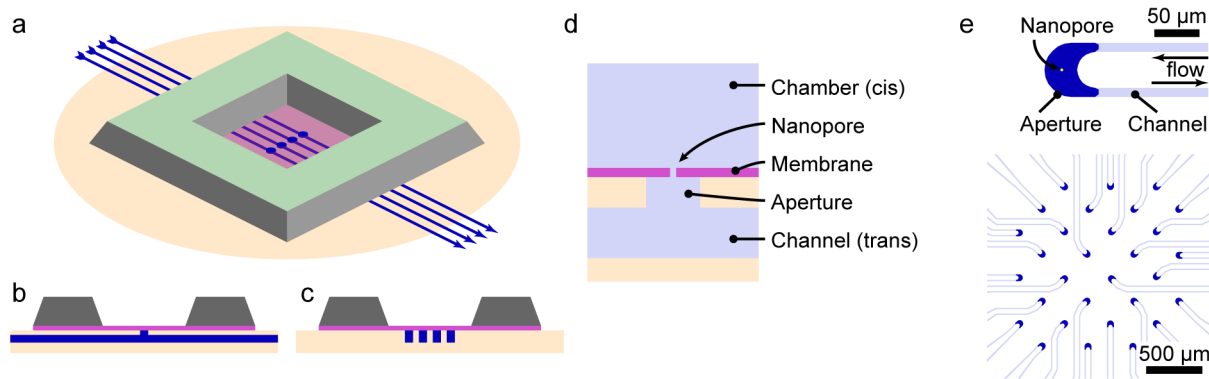


Figure 1: Concept. **a:** An isometric illustration showing nanopores in individual microfluidic channels. Only four channels are shown for simplicity. A nanopore membrane chip with a large window is bonded to microfluidic channels. **b:** A cross-section along a channel, showing an aperture in the channel enclosed by the nanopore membrane. **c:** A cross-section perpendicular to the channels, showing four apertures enclosed by the nanopore membrane. **d:** A magnification of (b), indicating the cis chamber and trans channel. **e:** Our design uses an out-and-back channels (above) to route all inflow and outflow channels for 30 nanopores in a  $2 \times 2$  mm<sup>2</sup> region (below).

## 2 Methods

### 2.1 Nanopore milling

Chips (5 mm square) with freestanding SiN<sub>x</sub> membranes were purchased from Silson Ltd. (Blisworth, England). Nanopores were produced by focused-ion-beam (FIB) milling using the gallium beam of an AURIGA CrossBeam FIB-SEM (Carl Zeiss AG, Oberkochen, Germany). Before milling, membranes were sputter coated with ~10 nm AuPd for conductivity. Nanopores were milled from the etched side of the nanopore chip to enable simple alignment to the membrane corners. The gallium beam was manually focused. Digital beam control held the focused beam (with a current of 1–20 pA) at a single location for up to 60 s to mill individual pores. Arrays were milled on  $2 \times 2$  mm<sup>2</sup> membranes and stage movement was used to produce an array over an area of  $1.4 \times 1.4$  mm<sup>2</sup>.

### 2.2 Microfluidic fabrication

Figure 2 illustrates the microfabrication methods. Microfluidic structures were produced by photolithography of a first spin-coated photoresist layer to define channels and a second dry film photoresist layer to enclose channels and define apertures. Glass substrates coated with silicon nitride were prepared by oxygen plasma treatment (2 min) and baking in an oven at 150 °C for 3 h. The channel layer of SU-8 was spin-coated to a nominal thickness of 10 μm (10 s at 500 rpm then 30 s at 1000 rpm) then baked on a hotplate for 1 min at 65 °C, 3 min at 95 °C and 1 min at 65 °C. The layer was patterned by UV exposure (430 mJ/cm<sup>2</sup>, i-line filter, MA6 mask aligner, SÜSS MicroTec AG). The post-exposure bake was 1 min at 65 °C, 5 min at 95 °C and 1 min at 65 °C. Substrates were developed in mr-Dev 600 (micro resist technology GmbH, Berlin, Germany) for 1 min, then rinsed with isopropanol and dried with nitrogen. Substrates were baked in an oven at 150 °C for 1 h for resistance against later exposure to cyclohexanone.

The aperture layer was formed by lamination of 20 μm-thick ADEX dry film resist (DJ Microlaminates, Sudbury, MA, USA). The film was laminated at 80 °C and 3 mm/s. The backing foil was removed before patterning by UV exposure (1000 mJ/cm<sup>2</sup> with i-line filter). The post-exposure bake was 1 min at 65 °C, 10 min at 85 °C and 1 min at 65 °C. Substrates rested for 2 h and then were developed in cyclohexanone for 3 min, rinsed with fresh cyclohexanone, rinsed with isopropanol and blow-dried with nitrogen with care to clear any solvents from the channels. The substrates were then ready for bonding with nanopore membranes.

### 2.3 Bonding

A dry bonding method was developed similar to Zhang et al. [2009]. We first modified nanopore membrane chips using an amino-based adhesion promoter as follows. Piranha solution was prepared by adding 1 part 30 % H<sub>2</sub>O<sub>2</sub> to 3 parts 96% H<sub>2</sub>SO<sub>4</sub>. Chips were submerged for 1 h, during which time the temperature remained above 100 °C. The surface of silicon nitride contains silicon oxide [Raider et al., 1976] and piranha cleaning forms silanol groups [Acres et al., 2012]. Piranha also removed the AuPd layer. Chips were then rinsed with deionized water and blown dry with nitrogen.

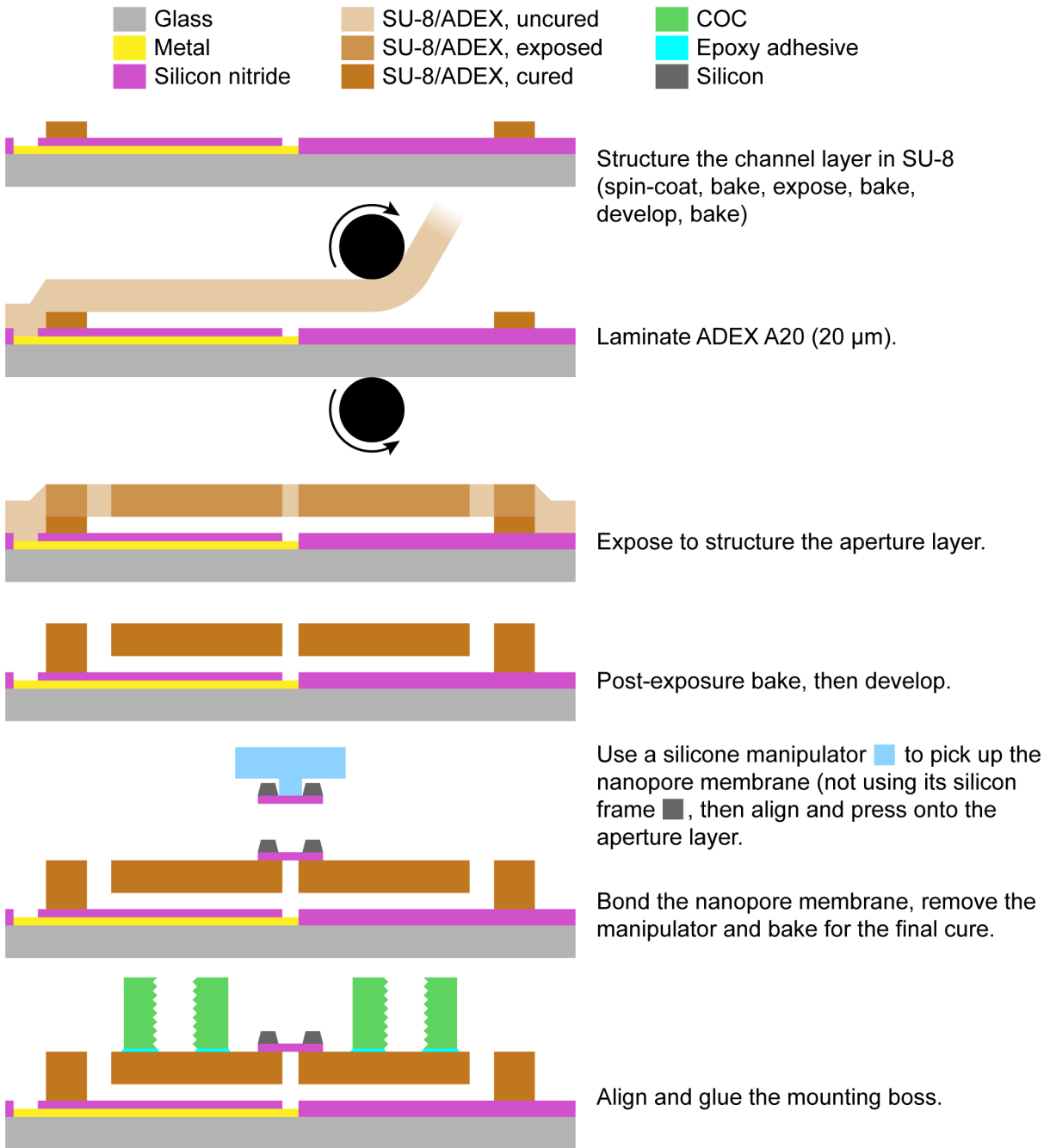


Figure 2: Fabrication scheme. Here, the fabrication of nanopore arrays is illustrated on a glass-based microelectrode array with a silicon nitride insulator. The same methods were used on glass substrates with unstructured silicon nitride coatings and no electrodes.

Membranes were coated with 3-aminopropyldimethylethoxysilane (APDMES) by immersion (overnight or longer) in a 1 % v/v solution in toluene. Finally, chips were rinsed with toluene, acetone, and isopropanol, dried with nitrogen, and baked in an oven at 120 °C for 30 min.

Nanopore membranes were bonded on the microfluidic aperture layer by a flip chip process (Finetech GmbH & Co. KG, Berlin, Germany). A custom silicone manipulator (1.9×1.9 mm<sup>2</sup>) picked up the membrane directly using van der Waals forces. We fluorinated the manipulator using 1H,1H,2H,2H-perfluorooctyltrichlorosilane to prevent chemical bonding to the membrane. The membrane and microfluidic apertures were optically aligned, then brought into contact. A force of 2–3 N was applied, and the temperature was increased at 1 °C/s to 100 C, held for 45 min, then decreased at the same rate; the manipulator was lifted from the membrane after returning to room temperature. Finally, substrates were hard-baked at 170 to 200 °C for several hours.

## 2.4 Microfluidic connectors

A connector was produced in a design adapted from Wagler et al. [2015] with inspiration from linear connectors from Dolomite Microfluidics. The connector consisted of silicone seals and a clamp, and additionally required a mounting boss on the microfluidic substrates. The clamp and mounting boss were produced by CNC-milling in aluminum and cyclic olefin copolymer (Topas 6015), respectively. The seals were produced by casting silicone (Sylgard 184) in a custom casting setup produced by CNC milling. Mounting bosses were glued to the substrates using an epoxy adhesive.

We used a casting setup like that of Wagler et al. to produce 30-channel silicone seals. A milled part with holes in a 2 mm pitch held metal needles (0.6 mm, Prym, Stolberg, Germany) to immobilize silicone tube ports (5 mm long, 0.51 mm inner diameter, VWR International GmbH, Darmstadt, Germany) in the casting setup. The tubes were activated by air plasma, the setup was filled with Sylgard 184 mixed at a 10:1 ratio, and the silicone was allowed to cure at room temperature to avoid shrinkage [Madsen et al., 2014].

## 2.5 Hydraulic resistance

For cylindrical channels, hydraulic resistance  $R_H$  was calculated by

$$R_H = \frac{128\eta L}{\pi d^4}$$

for a channel length  $L$  and diameter  $d$  and a dynamic viscosity  $\eta$  (0.89 mPa·s for water). For rectangular channels, the resistance was estimated as

$$R_H = \frac{12\eta L}{wh^3 \left(1 - \frac{0.63h}{w}\right)}$$

which is accurate to within about 13 % for square channels [Bruus, 2014].

To experimentally measure hydraulic resistance, we measured the time required for a meniscus to move a given distance in tubing of known diameter.

## 2.6 Measurement of nanopore arrays

For each nanopore, 2  $\mu$ L of phosphate-buffered saline (PBS) was injected through the inlet tube to fill the microfluidic channel until a droplet of PBS formed at the tip of the outlet tube. A 1 mL syringe containing PBS and a trans electrode was brought into contact with the outlet tube droplet (Figure 5a). The cis electrode was placed in the common bath above the nanopore membrane. Electrochemical impedance spectroscopy (EIS) was performed using a potentiostat (Bio-Logic Science Instruments SAS, Claix, France). Afterwards, the channel was flushed with 2  $\mu$ L of deionized water and finally pressurized air. This process was repeated for each channel. Flow was controlled by application of 1 bar of air pressure with a Luer-Lock blunt needle (outer diameter 0.8 mm) connected to each tube using a short segment of silicone tube. Before measurement, the nanopore array was treated with air plasma for 2 min to improve hydrophilicity. All electrodes were Ag/AgCl wire electrodes.

We use the following expression from Kowalczyk et al. [2011] to relate conductance  $G$  to diameter  $d$  and length  $l$  of a nanopore filled with a salt solution with conductivity  $\sigma$ :

$$G = \sigma \left[ \frac{4l}{\pi d^2} + \frac{1}{d} \right]^{-1} \quad (1)$$

## 2.7 Simulated electrical measurements

To predict the sensing capabilities of nanopores integrated in microfluidics, we simulated noise and translocation signals using an electrical circuit model and dimensions of a model nanopore.

### 2.7.1 Estimation of power spectral density

The power spectral density (PSD,  $S_i$ ) of a nanopore measurement was estimated as the sum of five components [Tabard-Cossa, 2013, Fragasso et al., 2020].

Flicker noise was calculated by

$$S_{1/f}(f) = \frac{\alpha_H I^2}{N_c f^\beta}$$

from the Hooge parameter  $\alpha_H$ , current  $I$ , number of charge carriers  $N_c$ , frequency  $f$  and empirical exponent  $\beta$ .

Thermal noise was

$$S_{\text{thermal}}(f) = \frac{4k_B T}{R}$$

with the Boltzmann constant  $k_B$ , temperature  $T$  and nanopore resistance  $R$  [Kowalczyk et al., 2011].

Shot noise was calculated as

$$S_{\text{shot}}(f) = 2Iq$$

with the current  $I$  and effective charge of current carrying species  $q$ .

Dielectric noise was calculated as

$$S_{\text{dielectric}}(f) = 8\pi k_B T C_{\text{chip}} D f$$

with the chip capacitance  $C_{\text{chip}}$ , dielectric loss  $D$ .

Capacitive noise was calculated as

$$S_{\text{capacitance}}(f) = 4\pi^2 C_{\text{total}}^2 v_n^2 f^2$$

with the total capacitance  $C_{\text{total}}$  and input voltage noise  $v_n$ .

### 2.7.2 Calculation of time series from power spectral density

The relationship between the PSD  $S_i$  and the Fourier transform ( $\mathcal{F}$ ) [The MathWorks, Inc., 2024] is

$$S_i(f) = \frac{|\mathcal{F}(I(t))|^2}{N f_s}$$

where  $N$  is the number of points in the time signal, and  $f_s$  is the sample rate. The Fourier transform of the time signal can then be found by

$$\mathcal{F}(I(t)) = \sqrt{N S_i(f) f_s}$$

As the PSD lacks phase information, we generate a random phase  $\theta$  for each frequency, with  $\theta = e^{ix}$  and  $x$  having a random value between 0 and  $2\pi$ .

To produce a current-time series, we then take the inverse real fast Fourier transform of the product of  $\mathcal{F}$  and  $\theta$ . This signal has a noise profile matching the original PSD.

### 2.7.3 Current blockade estimation using SPICE

Simulations of electrical circuit model for the nanopore were performed using LTSPICE XVII and python 3.11 using the circuit from 7. The blockade was modeled as the addition of a resistance  $\Delta R$  in equation 1 according to Kowalczyk et al. [2011]:

$$d_{\text{blockade}} = \sqrt{d_{\text{pore}}^2 - d_{\text{DNA}}^2}$$

and the diameter of double-stranded DNA of 2.2 nm.

## 3 Results

We present results showing that we could produce nanopore arrays and measure integrated nanopores. We also present calculations predicting the reduced noise of nanopores integrated by our methods.

### 3.1 Fabrication and stability

Our design (Figure 3) had 30 out-and-back microfluidic channels extending from peripheral access ports to a central nanopore region. In the nanopore region, microfluidic channels had a width of 10  $\mu\text{m}$  and a minimum distance between channels of 40  $\mu\text{m}$ . Peripherally, the channel width increased to 50  $\mu\text{m}$  to reduce hydraulic resistance. Channels had a height of 10  $\mu\text{m}$  and were enclosed by the 20  $\mu\text{m}$ -thick aperture layer. Neither collapse of the aperture layer nor bulging under pressure of up to 6 bar was observed. The aperture layer defined a crescent-shaped aperture (35  $\mu\text{m}$  across) in each channel (Figure 3f). The apertures' crescent shape and low height/width ratio were intended to reduce the risk of trapping bubbles (Figure 3b,c). When filled with water, no air bubbles were observed in the apertures.

When filled with water, we measured hydraulic resistances for single channels on the order of 15 kPa·s/nL, which matched predicted values. That is, pressure of 15 kPa would produce a flow rate of 1 nL/s. Pressure of 100 kPa (1 bar) would produce a flow of 7 nL/s or 400 nL/min. The volume of each microfluidic channel was on the order of 10 nL.

Nanopores milled by a 10 pA gallium beam for 30 s had diameters of <200 nm in 500 nm-thick membranes. The hydraulic resistance of such a nanopore is on the order of  $10^5$  kPa·s/nL. Alignment marks to enable optical alignment for bonding were also milled by the gallium beam.

Dry bonding of silicon nitride membranes to the microfluidic apertures formed a strong bond with a uniform appearance across most of the 2 mm membrane, except for unbonded peripheral regions (3d,e). Alignment precision was approximately 10  $\mu\text{m}$ . During application of up to 6 bar for flow in the microfluidic channels, the membrane at the aperture (at the halfway point of the channel) should have experienced a pressure of 3 bar. No detachment was observed. Higher pressures were not evaluated.<sup>1</sup>

In our bonding process, we manually brought the membrane into contact with the top of the aperture layer, using a vertical displacement lever on the FINEPLACER bonder and relying only on unmagnified visual observation from the side. Unsurprisingly, this process produced varying results. About half of bonded membranes were damaged, ranging from fracture around the perimeter of the membrane (which allowed removal of the Si frame) to shattering across the entire membrane. Unbroken membranes showed homogeneous bonding across the 1.9 mm region contacted directly by manipulator (Figure 3d). Interference patterns at the perimeter of the membrane and under the silicon frame (when viewed from the bottom) showed that the frame itself was not bonded.

The broken membranes however further demonstrated the strength of the bond. A membrane which shattered during bonding showed good adhesion even with high pressure applied to an aperture with a crack within 20  $\mu\text{m}$  (3g,h).

We observed no deterioration of the microfluidic channels or membranes when exposed to water for at least 2 weeks, neither after rinsing with isopropanol, ethanol or acetone or blowing with pressurized air. An ultrasonic bath shattered the free-standing regions of 500 nm-thick membranes.

### 3.2 Sixty-channel connector and fluidic handling

The connector (Figure 4) included two silicone seals, each capable of clamping 30 tubes (with a pitch of 2 mm in two offset rows of 15), held by an aluminum clamp. A tight fit was achieved by tubes with an outer diameter of 0.8 mm

<sup>1</sup>One exception: in an early experiment, we applied pressure by hand with a 1 mm syringe. The flow rate was high and uncontrolled, and generated extreme pressure which detached the membrane.

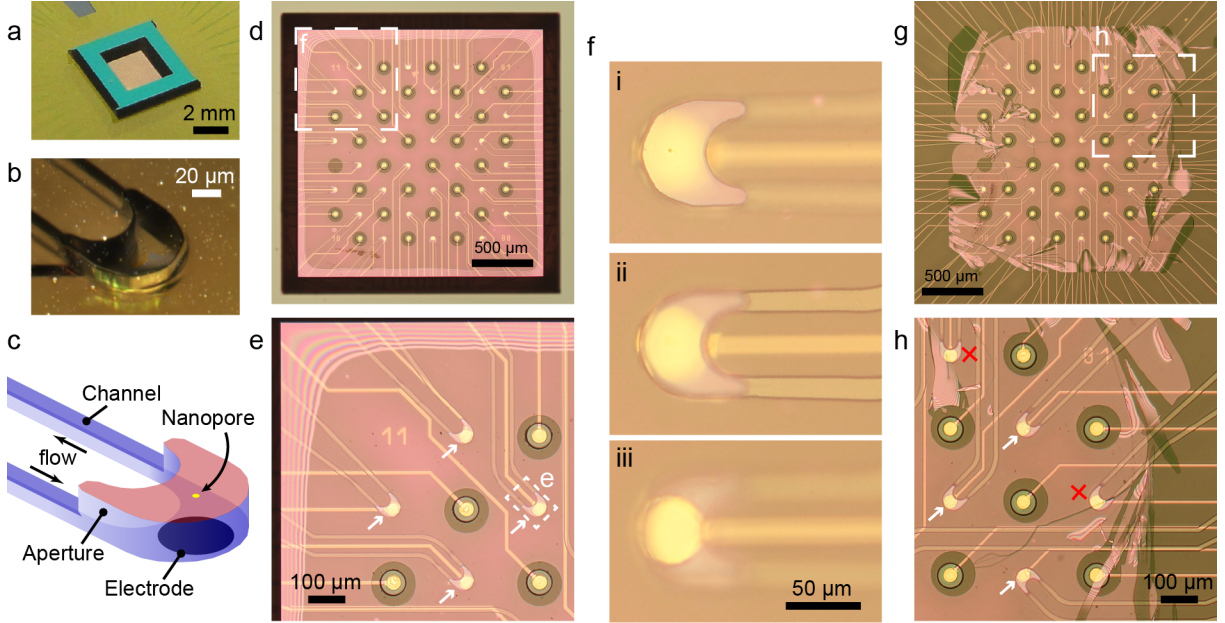


Figure 3: Nanopore array devices. **a:** Photo of a nanopore array with a  $2 \times 2 \text{ mm}^2$  membrane (in a  $5 \times 5 \text{ mm}^2$  chip) bonded to a microfluidic network. **b:** Oblique microscope photo (focus stack) of a single nanopore site. **c:** Oblique illustration of the aperture/nanopore region of a microfluidic channel. Channel: blue. Membrane: red. Nanopore: yellow. Electrode: black. **d, e:** Microscopic images of the nanopore array region. The silicon nitride membrane is  $2 \times 2 \text{ mm}^2$ . The etched slopes of the silicon chip appear black. Interference patterns indicate the unbonded region at the perimeter of the membrane, while the dark region (ca.  $1.9 \times 1.9 \text{ mm}^2$ ) is homogeneously bonded to the microfluidic layer. In (e), white arrows indicate four free-standing SiN membranes with nanopores. **f:** Magnification of a single channel with focus at (i) the nanopore membrane (the location of the nanopore appears as a dark spot), (ii) the microfluidic channel and (iii) the microelectrode. **g, h:** Microscopic images of a membrane which fractured during bonding. Fracture at the perimeter of the membrane detached the silicon frame. In comparison to the bonded regions, unbonded regions appear darker or show bright interference patterns. In (h), white arrows indicate three undamaged free-standing membranes (white arrows) and red x's indicate two damaged regions.

(fluorinated ethylene propylene,  $75 \text{ }\mu\text{m}$  inner diameter, IDEX H&S, Wertheim-Mondfeld, Germany). A mounting boss, permanently glued to each microfluidic substrate (4c), ensured precise alignment of the 60 tubes. The inner well of the boss defined the cis compartment for all nanopores.

The 60-channel microfluidic connector formed a reliable connection to the microfluidic chip. A good seal of the silicone seals against the transparent substrate was visually observed from below. We observed an absence of leakage by applying air pressure of up to 600 kPa while submerging the connector and chip under water.

### 3.3 Electrical measurements

The setup and its circuit model are illustrated in Figure 5, with estimated values in Table 2. Figure 6 shows measurements from a representative device. Eighteen nanopores were measured and showed expected resistive behavior at low frequencies. Fourteen showed similar conductances of  $25 \pm 3 \text{ nS}$  (resistance  $40 \text{ M}\Omega$ ), while four channels had lower conductances which we attribute to partial blockages in the microfluidic channels or tubing. Twelve nanopores were not measured due to blockages which prevented filling of the microfluidic channels.

### 3.4 Simulated electrical measurements

Our experimental demonstration used large nanopores, whereas most sensing applications require diameters far smaller than the  $20 \text{ nm}$  that is possible using a gallium FIB. To evaluate the effect of microfluidic integration on nanopore sensing, we performed simulations using a model circuit (Figure 7) and a model nanopore with a diameter of  $10 \text{ nm}$ . The resistor  $\Delta R$  represents the change of resistance during a translocation. Full details are in Table 3.

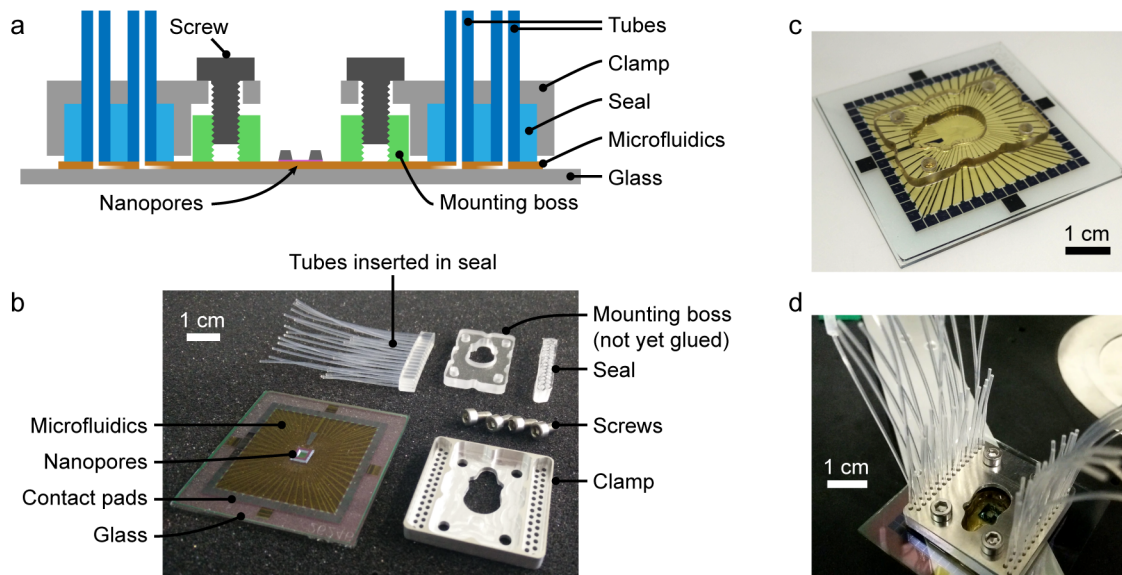


Figure 4: Microfluidic connector for the nanopore array. a: Schematic cross-section. b: Nanopore array device and disassembled connector parts. c: Nanopore array with glued mounting boss. d: Nanopore array assembled with connector. In the top left, a thicker silicone tube is connected to a single tube.

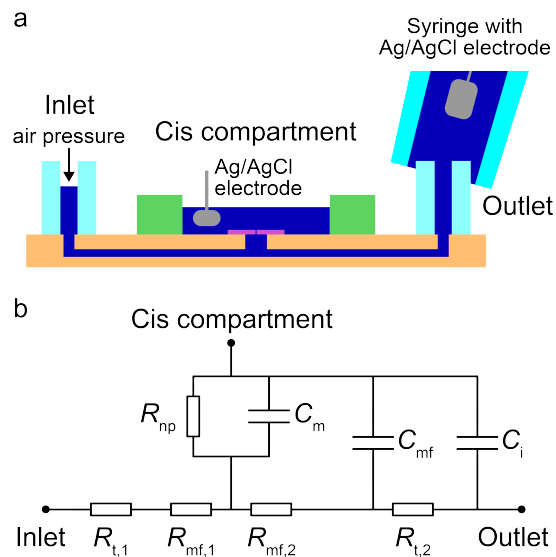


Figure 5: Set-up for measurements of nanopore arrays. a: Simplified schematic, not to scale. Measurements were made between Ag/AgCl electrodes in the cis compartment and the outlet. The outlet tube was loosely inserted into a syringe containing an electrode. Filling of the microfluidic channel was controlled by air pressure at the inlet tube. b: A circuit model of a single microfluidic channel and nanopore ( $R_{np}$ ). The microfluidic channel is divided into two components ( $R_{mf,1}$  and  $R_{mf,2}$ ) on either side of the nanopore; in our design, these components are roughly equal when both are filled. The resistance of the inlet and outlet tubes are  $R_{t,1}$  and  $R_{t,2}$ , respectively. The inlet tube is connected to pressurized air ( $R_{t,1} \rightarrow \infty$ ) and therefore measurements are made at the outlet. Importance capacitances are those of the membrane ( $C_m$ , pink in panel a), the microfluidic channel ( $C_{mf}$ , determined by the length of the channel in contact with the cis compartment), and the internal capacitance of the measurement electronics ( $C_i$ ).

Table 2: Estimated values for circuit elements of the integrated nanopores. Sources: relative permittivity of SiN [Piccirillo and Gobbi, 1990]; relative permittivity of ADEX is assumed to be similar to SU-8 [Ghannam et al., 2009]; conductivity of PBS measured to be 1.5 S/m.

Element	Value	Details
$R_{np}$	14 M $\Omega$	Diameter 200 nm, length 500 nm
$C_m$	0.3 pF	500 nm-thick SiN membrane, relative permittivity of 7, aperture area of 2500 $\mu\text{m}^2$
$C_{mf}$	0.2 pF	20 $\mu\text{m}$ -thick ADEX, relative permittivity of 2.85, channel area of 0.2 $\text{mm}^2$
$C_i$	20 pF	Parasitic capacitance
$R_{t,1}, R_{t,2}$	6 M $\Omega$	Diameter 75 $\mu\text{m}$ , length 4 cm
$R_{mf,1}, R_{mf,2}$	15 to 24 M $\Omega$	Channel lengths 15–21 mm, height 15 $\mu\text{m}$ , widths 10–50 $\mu\text{m}$
$R_{np} + R_{mf,2} + R_{t,2}$	35 to 44 M $\Omega$	

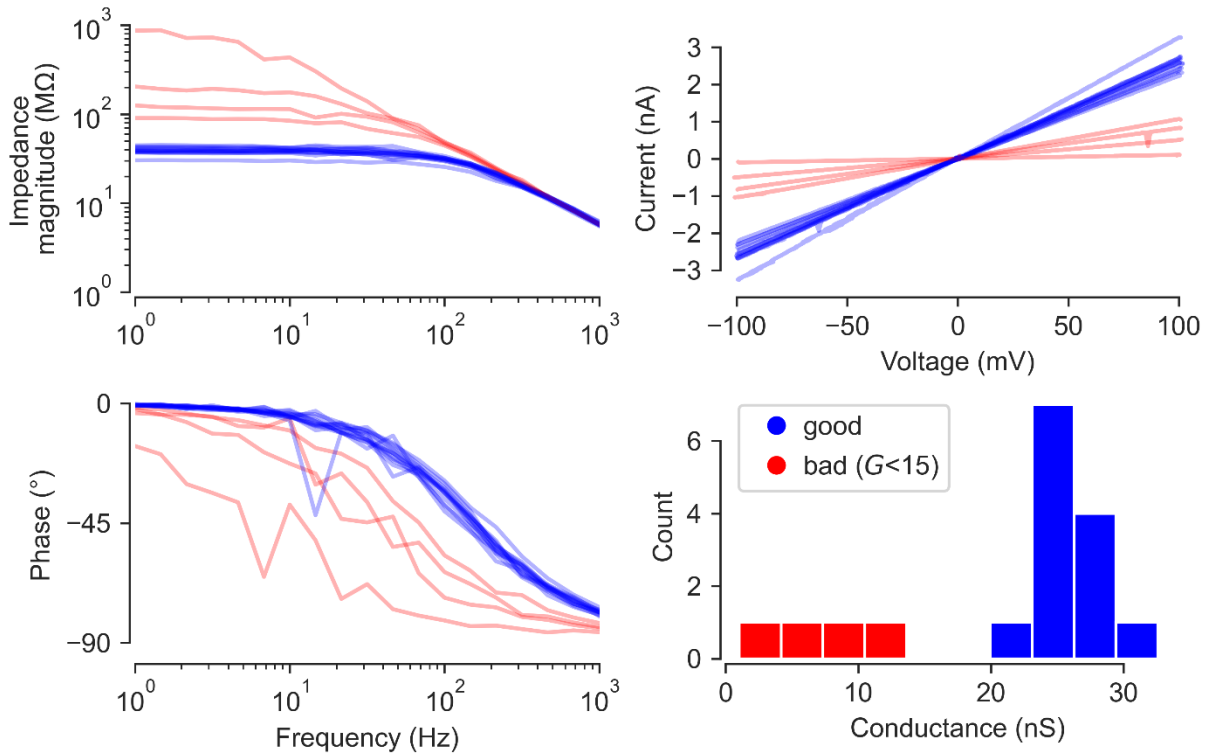


Figure 6: Electrochemical measurements of a nanopore array. Seventeen nanopores were measured, of which 13 (blue) exhibited expected conductances which included the series resistance of the microfluidic channel. Four nanopores exhibited low conductances (red). Left: Bode plots of impedance measurements. Right: Current–voltage plots and a conductance histogram.

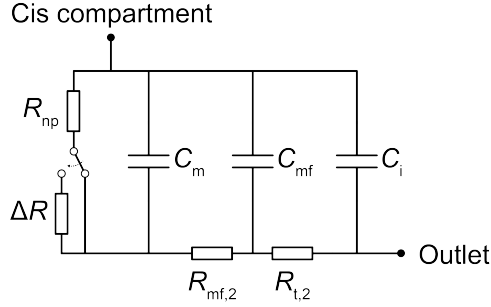


Figure 7: Circuit for simulations.

Table 3: Values for simulations.

Element	Value	Details
$\sigma$	10.5 S/m	1 M KCl
$R_{np}$	130.8 M $\Omega$ (open)	Open diameter 10 nm, length 100 nm (Equation 3)
$R_{np} + \Delta R$	137.2 M $\Omega$ (blocked)	Double-stranded DNA diameter of 2.2 nm
$C_m$	1.55 pF	100 nm-thick SiN membrane, relative permittivity of 7, aperture area of 2500 $\mu\text{m}^2$
$C_{mf}$	0.2 pF	20 $\mu\text{m}$ -thick ADEX, relative permittivity of 2.85, channel area of 0.2 $\text{mm}^2$
$C_i$	1 pF	Internal capacitance of the Axopatch 200B Molecular Devices, LLC [2012]
$R_{t,2}$	172 k $\Omega$	Diameter 75 $\mu\text{m}$ , length 8 mm, $\sigma$
$R_{mf,2}$	1.905 to 13.33 M $\Omega$	Channel lengths 15–21 mm, height 15 $\mu\text{m}$ , widths 10–50 $\mu\text{m}$ . 1.905 M $\Omega$ used in most simulations unless otherwise noted.
$R_{np} + R_{mf,2} + R_{t,2}$	138 to 150 M $\Omega$	
$f$	0.1 to 4 MHz	
$f_c$	100 kHz	Second-order Bessel filter
$T$	298 K	
$V$	500 mV	
$V_n$	3 nV/Hz $^{-1}$	Molecular Devices, LLC [2012]
$D$	10 $^{-3}$	Pan et al. [2023]

First, we calculated the noise expected in a nanopore measurement. Figure 8 shows the noise PSD, including the constituent components and total (left). Notably, this theoretical PSD is not limited to any bandwidth. To produce a more realistic PSD, the total PSD was transformed into a time-domain current trace, filtered using a 100 kHz low-pass filter, and a new PSD was calculated (Figure 8, right).

Next, we examined the shape of ionic current blockades. Blockade depth was calculated for double-stranded DNA. Blockade durations of 10  $\mu\text{s}$ , 100  $\mu\text{s}$  and 1 ms were considered. Simulations predict that microfluidic integration will filter the recordings due to additional series resistance (Figure 9). Specifically, the simulations varied  $R_{mf,2}$  from 0.1 to 8 M $\Omega$ . The high resistance corresponds to the use of an external electrode which accesses the nanopore via a microfluidic channel. The low resistance corresponds to a device in which an electrode is integrated in the proximity of a nanopore.

The effect of series resistance is contrasted in the first two rows, showing blockades with series resistances of 8 M $\Omega$  and 0.1 M $\Omega$ , respectively. Blockades with a 1 ms duration are well resolved. However, the 100  $\mu\text{s}$  blockade in the top row is distorted due to the high series resistance. The effect is stronger for 10  $\mu\text{s}$  blockades: the unfiltered blockade with low resistance (green) is nearly rectangular, while the unfiltered blockade with high resistance (blue) is significantly distorted. The effect of the 100 kHz low-pass filter becomes significant for such short pulses (orange and red).

In both rows, grey traces include noise simulated using SPICE. Noise was calculated for an open pore and does not consider the slight changes in noise during a blockade.

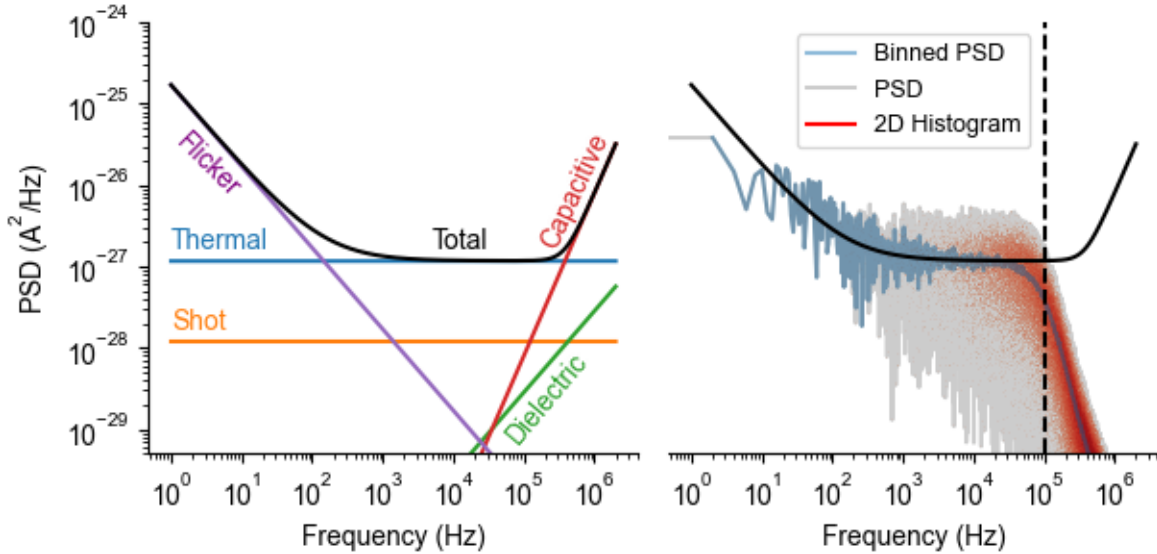


Figure 8: Theoretical PSD of a microfluidic-integrated nanopore. Left: Total noise was calculated from contributions of flicker, thermal, shot and capacitive noise. Dielectric noise was negligible. Right: A more realistic PSD was calculated from a theoretical low-pass filtered current trace. The dashed vertical line indicates the 100 kHz filter. The PSD (grey) is additionally plotted using logarithmic binning (blue) and a 2D histogram (red). The total PSD from the left panel is overlaid (black).

The third and fourth rows of Figure 9 illustrate this effect for a range of resistances, first unfiltered and then with a 100 kHz low-pass filter.

These results demonstrate that close integration between electrodes and nanopores will be important for high bandwidth measurements. Moreover, these results show that the filtering caused by a high series resistance is qualitatively similar to a low-pass filter. Interpretation of measurements using integrated nanopore devices must consider both effects.

## 4 Discussion

Here, we contrast our fabrication methods with previous work. We then focus on limitations of our devices (especially handling and usability). We also discuss noise.

### 4.1 Fabrication of nanopore array devices

Microfluidic integration of single nanopores or arrays of up to eight nanopores has previously been achieved using PDMS microfluidics [Jain et al., 2013, 2017, Tahvildari et al., 2015, 2016]. Thin film microfluidics as reported here would be challenging in PDMS, due to its flexibility. Furthermore, its ability to absorb small molecules makes it undesirable [Toepke and Beebe, 2006]. Therefore, we were motivated to integrate nanopores in epoxy photoresists to achieve thin layers and high resolution, thereby enabling higher nanopore density. Epoxy photoresists have proven suitable for nanopore sensing applications and use with Ag/AgCl microelectrodes in microelectrode cavity array (MECA) devices [Baaken et al., 2008]. ADEX is chemically similar to SU-8, and both can withstand solvents including ethanol, isopropanol, and acetone. Photolithographic patterning of epoxy resists could be extended to wafer-scale processes and CMOS wafers.

A challenge was to develop clean enclosed channels covered by ADEX. Without rinsing, residue remained in the channels. And without blow-drying, solvent remained in the channels. In our design, the central apertures enabled manual rinsing with fresh solvent followed by blow-drying with nitrogen, which achieved clean, dry channels. However, such manual rinsing and drying will not be possible when scaling to wafer-scale production with many chip replicates per wafer.

Previous reports of integration in PDMS microfluidics have contacted nanopore membranes from both sides, so that chemical bonding is additionally physically supported. A single-sided bonding method makes interfacing simpler but

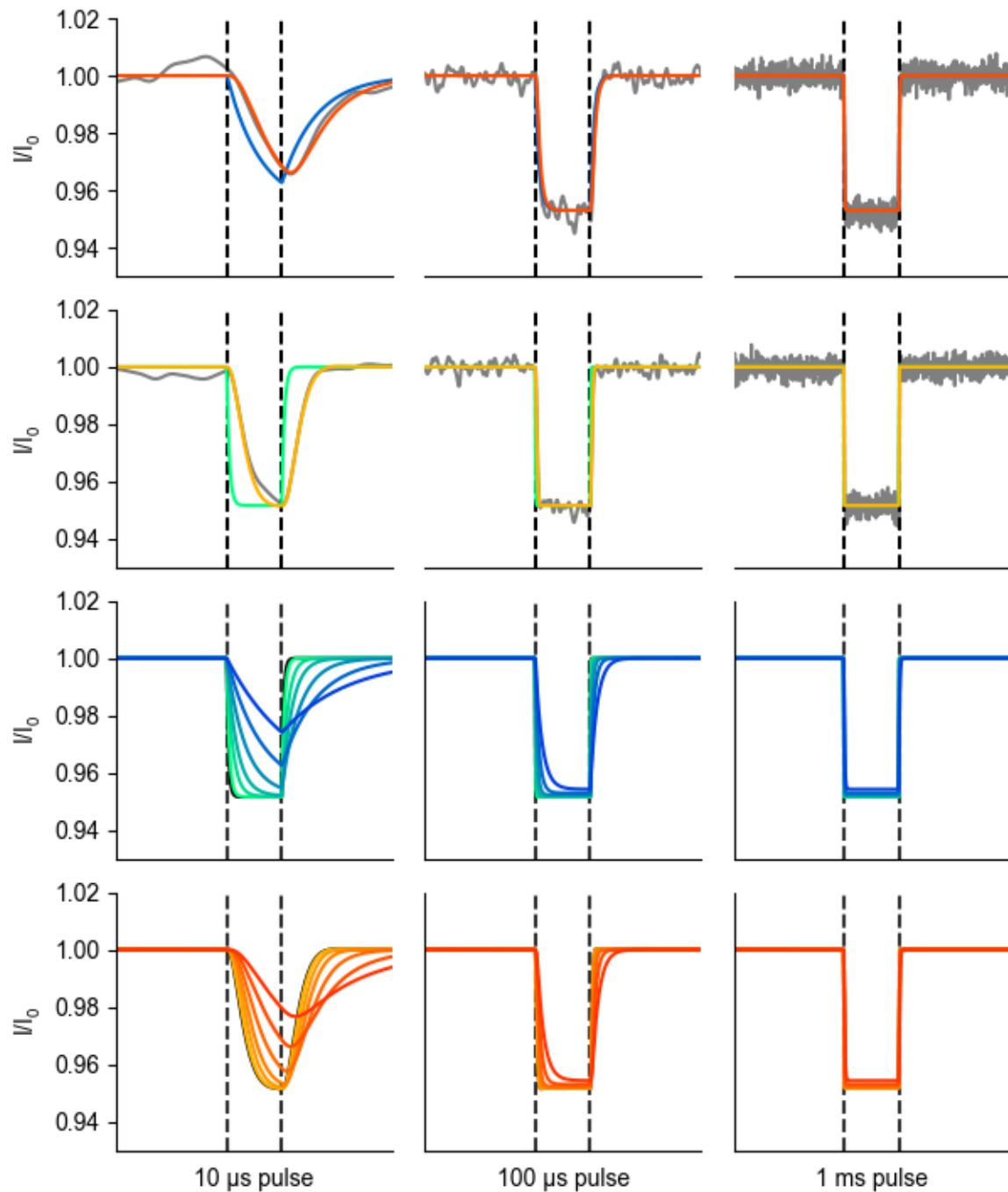


Figure 9: Effect of series resistance on translocation measurements. Microfluidic integration can filter recordings due to addition of a series resistance. First row: Simulated pulses filtered due to integration in a high resistance ( $8\text{ M}\Omega$ ) microfluidic channel (blue), additionally filtered by the  $100\text{ kHz}$  lowpass filter of the AxoPatch 200B (red) and with simulated noise (grey). Second row: Simulated pulses filtered due to integration in a low resistance ( $0.1\text{ M}\Omega$ ) microfluidic channel (green), additionally filtered by the  $100\text{ kHz}$  lowpass filter of the AxoPatch 200B (orange) and with simulated noise (grey). Third row: Simulated pulses filtered due to integration in microfluidic channels having resistances from  $0.1\text{ M}\Omega$  (green) to  $8\text{ M}\Omega$  (blue). Fourth row: The traces from the third row, additionally filtered by the  $100\text{ kHz}$  lowpass filter of the AxoPatch 200B. Simulated pulses have durations of  $10\text{ }\mu\text{s}$ ,  $100\text{ }\mu\text{s}$  and  $1\text{ ms}$  (left to right).

cannot rely on physical support. Therefore, we developed a dry bonding method based on amine–epoxide polyaddition. Similar methods have previously been reported for bonding of SU-8 and PDMS [Zhang et al., 2009, 2011, Watts et al., 2012], by exploiting residual epoxy groups in SU-8 and functionalization of PDMS with primary amine groups. The soft elastomeric nature of PDMS enabled good contact with comparably rigid SU-8. We believe that our successful bonding results were possible by supporting the flexible yet fragile SiN membrane on a soft silicone manipulator, and softening of the ADEX layer at elevated temperatures (before the later hard-bake to complete cross-linking). We expect that our roughly 50% chance of fracturing the membrane can be decreased with better process control, although this must be further investigated for thinner membranes.

In our bonding process, force could be roughly controlled with a weighted arm. Several membranes bonded with a force of 5 N shattered. At forces of 2–3 N, about half of the membranes shattered while the other half remained undamaged. We expect that the variability could be improved by magnified visualization during the bonding process or by improved force sensing and control. In some cases, the membrane was bonded while the Si frame cleanly broke off – similar results can be intentionally achieved by perforation of the membrane [Jain et al., 2013]. In cases where cracks in the SiN membrane were near ( $\sim 20\ \mu\text{m}$ ) but not contacting an aperture, we applied pressure of several bar and observed no weakness. We also expect that bonding may be achieved much faster than the 45 min used here.

For dry bonding of nanopore membranes, we chose the monofunctional APDMES, because common trifunctional silanes (such as aminopropyltriethoxysilane, APTES) can form thick layers [Vandenberg et al., 1991] which could block nanopores. The SiN membranes shatter in an ultrasonic bath which is often used to remove loosely bonded molecules. Electrical measurements confirmed that nanopores were unblocked after APDMES coating and bonding, although an organosilane coating does reduce nanopore size [Wanunu and Meller, 2007].

Further developments of adhesive bonding may be necessary for other membrane materials. New methods capable of orthogonally functionalization of the bonding regions of a membrane and the interior nanopore walls may also be needed for specific sensing capabilities.

We have also bonded nanopore arrays using a liquid adhesive [Kentsch et al., 2006]. The liquid adhesive risked filling the channels or nanopores, and even in successful cases extended a meniscus 10–20  $\mu\text{m}$  along the membrane into the apertures. In comparison, dry bonding caused no deformation of the microfluidic structures.

We produced large nanopores using a gallium FIB, which readily patterns nanopores over large areas but cannot achieve nanopores smaller than 20 nm. Our nanopore arrays were patterned in a 1.4 mm square, which is beyond the field of view of conventional transmission electron microscopes. Milling with a helium ion beam would enable large arrays with nanopore sizes competitive with electron beam milling. We also produced alignment marks using the gallium beam, which would be impractical with an electron or helium beam, and should rather be produced lithographically. Rather than milling nanopores, controlled breakdown avoids the need for precise bonding alignment [Tahvildari et al., 2015]. Nanopore fabrication by reactive-ion etching may be beneficial for scale-up [Bai et al., 2014, Martens et al., 2022].

## 4.2 Electrical properties of nanopore arrays

In our work, we estimated (Table 2) that the capacitance of a suspended membrane was 0.3 pF, and that the microfluidic channel added a capacitance of 0.2 pF. These capacitances must be minimized to limit current noise. The 20 pF internal capacitance of the potentiostat prevented better analysis of these capacitances.

The 500 nm thickness of our membranes limits comparison with other nanopores. We estimate a 20 nm-thick membrane suspended over the microfluidic apertures would have a capacitance of about 10 pF – much higher than desired. Good solutions would be to have thinned regions on a thick membrane (which would also facilitate handling and bonding) and to reduce the aperture size. We have produced apertures as small as 6  $\mu\text{m}$  in 20  $\mu\text{m}$ -thick ADEX, although such high aspect ratio features may trap bubbles and are sensitive to process fluctuations. For smaller apertures, we expect good results would be possible using 5  $\mu\text{m}$ -thin ADEX.

The effect of the high resistances of the microfluidic channels and tubes on sensing capabilities should be investigated in future work. Integration of Ag/AgCl microelectrodes near the nanopores and the use of 3- or 4-electrode systems could be considered.

## 4.3 Fluidic handling

Future nanopore devices should be simple and easy to use, however this was not achieved in this work. Although we solved the challenge of connecting 60 tubes to a microfluidic chip, handling 30 channels remains challenging and flow control was done serially in all channels. Neither syringe pumps nor pressure-driven pumps are readily available in 30-channel formats.

Each channel required two tubes, as interfacing to a nanopore generally requires a channel having both an inlet and an outlet. Nanopores themselves have enormous hydraulic resistances (Equation 1), so that filling or rinsing from a single inlet through the pore itself is impractical. Rinsing our microfluidic channels was slow (minutes per microliter), however rinsing through a nanopore would be much slower (weeks or months per microliter).

Our serial process for filling channels and measuring impedance spectra required about 12 min per nanopore, or >6 hours for the array. The low volume of the microfluidic channel (~10 nL) results in a residence time of water of about 1 s (at 1 bar). This suggests that handling 30 channels in a reasonable timeframe could be possible if a technical solution were developed. Directly pipetting into each channel would be convenient, however air cushioned pipettes apply low pressure and positive displacement pipettes would risk damaging the membranes due to high pressures. We're not aware of pressure-controlled pipettes which would make 30 channels possible (although laborious). Scaling would quickly become absurd. Overall, we believe that any devices with similar or higher numbers of nanopores require new microfluidic concepts to integrate multiple nanopores per microfluidic channel. An example would be multiplexing using microfluidic control valves [Tahvildari et al., 2016], although using materials other than PDMS would be desirable [Roy et al., 2011]. Future work could investigate on-chip sample processing [Varongchayakul et al., 2018] before read-out using nanopore arrays.

#### 4.4 Noise of integrated nanopores

Other groups have shown a reduction in noise using more highly integrated systems for measuring nanopores [Rosenstein et al., 2012]. Our results support this, and furthermore highlight the detrimental effect that electrical resistance of microfluidic channels may have.

The current noise PSD (Figure 8) showed that the low capacitance realized by microfluidic integration will minimize capacitive or dielectric noise at a bandwidth up to 100 kHz. Previous efforts have reduced capacitance by manually painting insulating silicone on nanopore membranes [Balan et al., 2014]. Compared to manually painting the insulating layer, the use of photolithographic microfabrication and dry bonding allows for a scalable and reproducible method for reducing the current noise of nanopores.

The presented microfluidic chip demonstrates the potential for low-noise, high-bandwidth measurements (well beyond 100 kHz). While SPICE simulations indicate that high series resistance in the microfluidic channels could impact signal quality, this challenge can be addressed with optimized design strategies. Reducing the electrical resistance of the microfluidic channels will enhance the performance of the nanopore device by minimizing signal attenuation at higher frequencies. Achieving a resistance below 1 M $\Omega$ , for instance, would enable resolution of short 10  $\mu$ s blockades. Moving forward, integrating microelectrodes close to the nanopores, along with the use of CMOS chips for on-site amplification and digitization, could further advance the capabilities of integrated microfluidic nanopore arrays

Beyond achieving low noise in high bandwidth measurements, our results highlight challenges for resolving short signals. SPICE simulations of ionic current blockades (Figure 9) demonstrate that the high series resistance introduced by a microfluidic channel between a nanopore and an electrode increases the RC time constant of the nanopore device, leading to signal attenuation at higher frequencies. Integrated nanopore arrays must minimize this resistance to enable high bandwidth measurements. For example, a resistance less than 1 M $\Omega$  would be necessary to resolve 10  $\mu$ s blockades. The ideal solution would be to integrate microelectrodes in direct proximity to the nanopores. Beyond the use of integrated microfluidic nanopore arrays on glass substrates, further improvement will be gained by direct integration on CMOS chips for amplification and digitization.

#### 4.5 Limitations of this work

A limitation of our work is the use of thick membranes and large nanopores. Our design required a grid of nanopores over an area of 1.4x1.4 mm<sup>2</sup>. We could easily pattern these nanopores and optically visible alignment marks using a gallium FIB. An array over such a large area using a TEM would be challenging. Future work should integrate alignment marks using RIE and produce nanopores using helium ion milling which can achieve single-digit nanometer diameters.

Stability of nanopores remains a concern [Chou et al., 2020]. Different membrane materials or coatings such as HfO<sub>2</sub> should improve nanopore stability, but their integration using our methods may require changes to bonding chemistry.

Our minimum microfluidic feature sizes of 10  $\mu$ m were straightforward to fabricate for this demonstration. Increasing resolution could easily increase channel/nanopore density, however handling is currently the limitation.

The integration of electrodes is another issue to be solved, and their size may limit nanopore array density. Our design included electrodes with a diameter of 30  $\mu$ m (which we did not use for measurements), similar to MECA chips for

biological nanopores [Baaken et al., 2008]. Integrated electrodes for solid-state nanopores may require diameters 10 times larger. If using glass substrates, aligning the nanopore over a window in the electrode would allow correlative optical measurements [Ensslen and Behrends, 2022].

## 5 Conclusions

We have presented a microfluidic chip featuring the largest number of individually-addressed solid-state nanopores to date. Our dry bonding method established a stable chemical bond between silicon nitride membranes and microfluidic networks, while enabling maximum process flexibility by separating nanofabrication and microfabrication processes. The method should be compatible with CMOS substrates containing integrated microelectrodes and alternative nanopore fabrication methods such as helium ion beam milling, reactive-ion etching or controlled breakdown. Measurements confirmed the electrical isolation of the integrated nanopores, and calculations demonstrated that integrated nanopores can enable recordings with reduced current noise. A major limitation is the impractical chip-to-world connection, which required 60 tubes for the 30 microfluidic channels. Simulations show that integration of electrodes near the nanopores will be necessary for high bandwidth measurements. Our fabrication method holds promise when applied to new designs that improve fluidic interfacing and electrode integration.

## 6 Acknowledgements

This work was supported by the European Commission (7th Framework Programme, Marie Curie Initial Training Network “NAMASEN,” contract n. 264872), the VW Foundation under their Experiment! Program, the State Ministry of Economic Affairs, Labour and Tourism as part of the Forum Gesundheitsstandort Baden-Württemberg (TechPat nano), and the Federal Ministry of Education and Research (BMBF) in the project nanodiag\_BW (03ZU1208BG).

## References

- R. G. Acres, A. V. Ellis, J. Alvino, C. E. Lenahan, D. A. Khodakov, G. F. Metha, and G. G. Andersson. Molecular structure of 3-aminopropyltriethoxysilane layers formed on silanol-terminated silicon surfaces. *The Journal of Physical Chemistry C*, 116(10):6289–6297, Mar. 2012. ISSN 1932-7447. doi:10.1021/jp212056s. URL <http://pubs.acs.org/doi/abs/10.1021/jp212056s>.
- G. Baaken, M. Sondermann, C. Schlemmer, J. Rühle, and J. C. Behrends. Planar microelectrode-cavity array for high-resolution and parallel electrical recording of membrane ionic currents. *Lab on a Chip*, 8(6):938–44, June 2008. ISSN 1473-0197. doi:10.1039/b800431e. URL <http://www.ncbi.nlm.nih.gov/pubmed/18497915>. ISBN: 7612035146.
- J. Bai, D. Wang, S.-w. Nam, H. Peng, R. Bruce, L. Gignac, M. Brink, E. Kratschmer, S. Rosnagel, P. Waggoner, K. Reuter, C. Wang, Y. Astier, V. Balagurusamy, B. Luan, Y. Kwark, E. Joseph, M. Guillorn, S. Polonsky, A. Royyuru, S. Papa Rao, and G. Stolovitzky. Fabrication of sub-20 nm nanopore arrays in membranes with embedded metal electrodes at wafer scales. *Nanoscale*, 6(15):8900–8906, 2014. ISSN 2040-3364, 2040-3372. doi:10.1039/C3NR06723H. URL <http://xlink.rsc.org/?DOI=C3NR06723H>.
- A. Balan, B. Machielse, D. Niedzwiecki, J. Lin, P. Ong, R. Engelke, K. Shepard, and M. Drndic. Improving signal-to-noise performance for DNA translocation in solid-state nanopores at MHz bandwidths. *Nano Letters*, Nov. 2014. ISSN 1530-6992. doi:10.1021/nl504345y. URL <http://www.ncbi.nlm.nih.gov/pubmed/25418589>.
- H. Bruus. Governing equations in microfluidics. In T. Laurell and A. Lenshof, editors, *Microscale Acoustofluidics*, pages 1–28. Royal Society of Chemistry, Cambridge, 2014. ISBN 978-1-84973-671-8. doi:10.1039/9781849737067-00001. URL <http://ebook.rsc.org/?DOI=10.1039/9781849737067>. ISSN: 1473-0197.
- Y.-C. Chou, P. Masih Das, D. S. Monos, and M. Drndic. Lifetime and Stability of Silicon Nitride Nanopores and Nanopore Arrays for Ionic Measurements. *ACS Nano*, page acsnano.9b09964, Apr. 2020. ISSN 1936-0851, 1936-086X. doi:10.1021/acsnano.9b09964. URL <https://pubs.acs.org/doi/10.1021/acsnano.9b09964>.
- D. Emmrich, A. Beyer, A. Nadzeyka, S. Bauerdick, J. C. Meyer, J. Kotakoski, and A. Götzhäuser. Nanopore fabrication and characterization by helium ion microscopy. *Applied Physics Letters*, 108(16):163103, Apr. 2016. ISSN 0003-6951, 1077-3118. doi:10.1063/1.4947277. URL <http://aip.scitation.org/doi/10.1063/1.4947277>.
- T. Ensslen and J. C. Behrends. A chip-based array for high-resolution fluorescence characterization of free-standing horizontal lipid membranes under voltage clamp. *Lab on a Chip*, 22(15):2902–2910, 2022. ISSN 1473-0197, 1473-0189. doi:10.1039/D2LC00357K. URL <http://xlink.rsc.org/?DOI=D2LC00357K>.

- A. Fragasso, S. Schmid, and C. Dekker. Comparing Current Noise in Biological and Solid-State Nanopores. *ACS Nano*, page acsnano.9b09353, Feb. 2020. ISSN 1936-0851, 1936-086X. doi:10.1021/acsnano.9b09353. URL <https://pubs.acs.org/doi/10.1021/acsnano.9b09353>.
- A. Ghannam, C. Viallon, D. Bourrier, and T. Parra. Dielectric microwave characterization of the SU-8 thick resin used in an above IC process. In *2009 European Microwave Conference (EuMC)*, pages 1041–1044, Rome, Italy, Sept. 2009. IEEE. ISBN 978-1-4244-4748-0. doi:10.23919/EUMC.2009.5295989. URL <https://ieeexplore.ieee.org/document/5295989/>.
- T. Jain, R. J. S. Guerrero, C. A. Aguilar, and R. Karnik. Integration of solid-state nanopores in microfluidic networks via transfer printing of suspended membranes. *Analytical Chemistry*, 85(8):3871–3878, Apr. 2013. ISSN 0003-2700. doi:10.1021/ac302972c. URL <http://www.ncbi.nlm.nih.gov/pubmed/23347165>.
- T. Jain, B. C. Rasera, R. J. S. Guerrero, J.-M. Lim, and R. Karnik. Microfluidic multiplexing of solid-state nanopores. *Journal of Physics: Condensed Matter*, 29(48):484001, Dec. 2017. ISSN 0953-8984, 1361-648X. doi:10.1088/1361-648X/aa9455. URL <https://iopscience.iop.org/article/10.1088/1361-648X/aa9455>.
- P. D. Jones. *Nanofluidic technology for chemical neurostimulation*. PhD, University of Tübingen, 2017. URL <http://dx.doi.org/10.15496/publikation-20363>.
- J. Kentsch, S. Breisch, and M. Stelzle. Low temperature adhesion bonding for BioMEMS. *Journal of Micromechanics and Microengineering*, 16(4):802–807, Apr. 2006. ISSN 0960-1317. doi:10.1088/0960-1317/16/4/017. URL <http://stacks.iop.org/0960-1317/16/i=4/a=017?key=crossref.dc14895103290ff182fd3fe47dff471>.
- S. W. Kowalczyk, A. Y. Grosberg, Y. Rabin, and C. Dekker. Modeling the conductance and DNA blockade of solid-state nanopores. *Nanotechnology*, 22(31):315101, Aug. 2011. ISSN 1361-6528. doi:10.1088/0957-4484/22/31/315101. URL <http://www.ncbi.nlm.nih.gov/pubmed/21730759>.
- A. H. Laszlo, I. M. Derrington, B. C. Ross, H. Brinkerhoff, A. Adey, I. C. Nova, J. M. Craig, K. W. Langford, J. M. Samson, R. Daza, K. Doering, J. Shendure, and J. H. Gundlach. Decoding long nanopore sequencing reads of natural DNA. *Nature Biotechnology*, (June):2–7, June 2014. ISSN 1087-0156. doi:10.1038/nbt.2950. URL <http://www.nature.com/doifinder/10.1038/nbt.2950>. Publisher: Nature Publishing Group.
- M. H. Madsen, N. A. Feidenhans'l, P.-E. Hansen, J. Garnæs, and K. Dirscherl. Accounting for PDMS shrinkage when replicating structures. *Journal of Micromechanics and Microengineering*, 24:127002, 2014. ISSN 0960-1317. doi:10.1088/0960-1317/24/12/127002. URL <http://stacks.iop.org/0960-1317/24/i=12/a=127002?key=crossref.15ed7dc09916ada004812299ec8e4555>.
- S. Magierowski, Y. Huang, C. Wang, and E. Ghafar-Zadeh. Nanopore-CMOS Interfaces for DNA Sequencing. *Biosensors*, 6(3):42, Aug. 2016. ISSN 2079-6374. doi:10.3390/bios6030042. URL <http://www.mdpi.com/2079-6374/6/3/42>.
- K. Martens, D. Barge, L. Liu, S. Santermans, C. Stoquart, J. Delpont, K. Willems, D. Ruic, S. Marion, J. Gevers, B. D. Bois, A. Andrei, L. Lagae, M. Veugelers, A. S. Verhulst, S. Severi, and P. V. Dorpe. The Nanopore-FET as a High-Throughput Barcode Molecule Reader for Single-Molecule Omics and Read-out of DNA Digital Data Storage. In *2022 International Electron Devices Meeting (IEDM)*, pages 17.4.1–17.4.4, San Francisco, CA, USA, Dec. 2022. IEEE. ISBN 978-1-66548-959-1. doi:10.1109/IEDM45625.2022.10019451. URL <https://ieeexplore.ieee.org/document/10019451/>.
- Molecular Devices, LLC. Axon Axopatch 200B Microelectrode Amplifier, 2012.
- Z. Pan, P. S. Barry, T. Cecil, C. Albert, A. N. Bender, C. L. Chang, R. Gualtieri, J. Hood, J. Li, J. Zhang, M. Lisovenko, V. Novosad, G. Wang, and V. Yefremenko. Measurement of Dielectric Loss in Silicon Nitride at Centimeter and Millimeter Wavelengths. *IEEE Transactions on Applied Superconductivity*, 33(5):1–7, Aug. 2023. ISSN 1051-8223, 1558-2515, 2378-7074. doi:10.1109/TASC.2023.3264953. URL <https://ieeexplore.ieee.org/document/10098857/>.
- A. Piccirillo and A. L. Gobbi. Physical-electrical properties of silicon nitride deposited by PECVD on III–V semiconductors. *Journal of The Electrochemical Society*, 137(12):3910–3917, 1990. ISSN 00134651. doi:10.1149/1.2086326. URL <http://doi.wiley.com/10.1002/chin.199108015>.
- S. I. Raider, R. Flitsch, J. A. Aboaf, and W. A. Pliskin. Surface oxidation of silicon nitride films. *Journal of The Electrochemical Society*, 123(4):560, 1976. ISSN 00134651. doi:10.1149/1.2132877. URL <http://jes.ecsdl.org/cgi/doi/10.1149/1.2132877>.
- J. K. Rosenstein, M. Wanunu, C. A. Merchant, M. Drndic, and K. L. Shepard. Integrated nanopore sensing platform with sub-microsecond temporal resolution. *Nature Methods*, 9(5):487–492, May 2012. ISSN 1548-7091, 1548-7105. doi:10.1038/nmeth.1932. URL <http://www.nature.com/articles/nmeth.1932>.

- E. Roy, J.-C. Galas, and T. Veres. Thermoplastic elastomers for microfluidics: Towards a high-throughput fabrication method of multilayered microfluidic devices. *Lab on a Chip*, 11(18):3193, 2011. ISSN 1473-0197, 1473-0189. doi:10.1039/c1lc20251k. URL <http://xlink.rsc.org/?DOI=c1lc20251k>.
- V. Tabard-Cossa. Instrumentation for Low-Noise High-Bandwidth Nanopore Recording. In *Engineered Nanopores for Bioanalytical Applications*, pages 59–93. Elsevier, 2013. ISBN 978-1-4377-3473-7. doi:10.1016/B978-1-4377-3473-7.00003-0. URL <https://linkinghub.elsevier.com/retrieve/pii/B9781437734737000030>.
- R. Tahvildari, E. Beamish, V. Tabard-Cossa, and M. Godin. Integrating nanopore sensors within microfluidic channel arrays using controlled breakdown. *Lab on a Chip*, 15:1407–1411, 2015. ISSN 1473-0197. doi:10.1039/C4LC01366B. URL <http://dx.doi.org/10.1039/C4LC01366B>. Publisher: Royal Society of Chemistry.
- R. Tahvildari, E. Beamish, K. Briggs, S. Chagnon-Lessard, A. N. Sohi, S. Han, B. Watts, V. Tabard-Cossa, and M. Godin. Manipulating electrical and fluidic access in integrated nanopore-microfluidic arrays using microvalves. *Small*, page 1602601, Dec. 2016. ISSN 16136810. doi:10.1002/sml.201602601. URL <http://doi.wiley.com/10.1002/sml.201602601>.
- The MathWorks, Inc. Power Spectral Density Estimates Using FFT, 2024. URL <https://de.mathworks.com/help/signal/ug/power-spectral-density-estimates-using-fft.html>.
- M. W. Toepke and D. J. Beebe. PDMS absorption of small molecules and consequences in microfluidic applications. *Lab on a Chip*, 6(12):1484, 2006. ISSN 1473-0197, 1473-0189. doi:10.1039/b612140c. URL <http://xlink.rsc.org/?DOI=b612140c>.
- E. T. Vandenberg, L. Bertilsson, B. Liedberg, K. Uvdal, R. Erlandsson, H. Elwing, and I. Lundström. Structure of 3-aminopropyl triethoxy silane on silicon oxide. *Journal of Colloid and Interface Science*, 147(1):103–118, 1991. ISSN 00219797. doi:10.1016/0021-9797(91)90139-Y. ISBN: 0021-9797.
- N. Varongchayakul, J. S. Hersey, A. Squires, A. Meller, and M. W. Grinstaff. A Solid-State Hard Microfluidic–Nanopore Biosensor with Multilayer Fluidics and On-Chip Bioassay/Purification Chamber. *Advanced Functional Materials*, 28(50):1804182, Dec. 2018. ISSN 1616-301X, 1616-3028. doi:10.1002/adfm.201804182. URL <https://onlinelibrary.wiley.com/doi/10.1002/adfm.201804182>.
- P. F. Wagler, U. Tangen, J. Ott, and J. S. McCaskill. General-purpose, parallel and reversible microfluidic interconnects. *IEEE Transactions on Components, Packaging and Manufacturing Technology*, 5(March):291–300, 2015. ISSN 2156-3950. doi:10.1109/TCPMT.2015.2395815. URL <http://ieeexplore.ieee.org/lpdocs/epic03/wrapper.htm?arnumber=7036123>.
- M. Wanunu and A. Meller. Chemically modified solid-state nanopores. *Nano Letters*, 7(6):1580–5, June 2007. ISSN 1530-6984. doi:10.1021/nl070462b. URL <http://www.ncbi.nlm.nih.gov/pubmed/17503868>.
- B. R. Watts, T. Kowpak, Z. Zhang, C.-Q. Xu, S. Zhu, X. Cao, and M. Lin. Fabrication and performance of a photonic-microfluidic integrated device. *Micromachines*, 3(4):62–77, Feb. 2012. ISSN 2072-666X. doi:10.3390/mi3010062. URL <http://www.mdpi.com/2072-666X/3/1/62/>.
- D. Xia, C. Huynh, S. McVey, A. Kobler, L. Stern, Z. Yuan, and X. S. Ling. Rapid fabrication of solid-state nanopores with high reproducibility over a large area using a helium ion microscope. *Nanoscale*, 10(11):5198–5204, 2018. ISSN 2040-3364, 2040-3372. doi:10.1039/C7NR08406D. URL <http://xlink.rsc.org/?DOI=C7NR08406D>.
- Z. Zhang, P. Zhao, and G. Xiao. The fabrication of polymer microfluidic devices using a solid-to-solid interfacial polyaddition. *Polymer*, 50(23):5358–5361, Nov. 2009. ISSN 00323861. doi:10.1016/j.polymer.2009.09.053. URL <http://linkinghub.elsevier.com/retrieve/pii/S0032386109008106>. Publisher: Elsevier Ltd.
- Z. Zhang, P. Zhao, G. Xiao, B. R. Watts, and C. Xu. Sealing SU-8 microfluidic channels using PDMS. *Biomicrofluidics*, 5(4):46503–465038, Dec. 2011. ISSN 1932-1058. doi:10.1063/1.3659016. URL <http://www.pubmedcentral.nih.gov/articlerender.fcgi?artid=3364813&tool=pmcentrez&rendertype=abstract>.